

## Facet recovery and light emission from GaN/InGaN/GaN core-shell structures grown by metal organic vapour phase epitaxy on etched GaN nanorod arrays

E. D. Le Boulbar, I. Gîrgel, C. J. Lewins, P. R. Edwards, R. W. Martin et al.

Citation: *J. Appl. Phys.* **114**, 094302 (2013); doi: 10.1063/1.4819440

View online: <http://dx.doi.org/10.1063/1.4819440>

View Table of Contents: <http://jap.aip.org/resource/1/JAPIAU/v114/i9>

Published by the AIP Publishing LLC.

---

### Additional information on J. Appl. Phys.

Journal Homepage: <http://jap.aip.org/>

Journal Information: [http://jap.aip.org/about/about\\_the\\_journal](http://jap.aip.org/about/about_the_journal)

Top downloads: [http://jap.aip.org/features/most\\_downloaded](http://jap.aip.org/features/most_downloaded)

Information for Authors: <http://jap.aip.org/authors>

## ADVERTISEMENT



**AIPAdvances**

Now Indexed in Thomson Reuters Databases

Explore AIP's open access journal:

- Rapid publication
- Article-level metrics
- Post-publication rating and commenting

# Facet recovery and light emission from GaN/InGaN/GaN core-shell structures grown by metal organic vapour phase epitaxy on etched GaN nanorod arrays

E. D. Le Boulbar,<sup>1</sup> I. Gîrgel,<sup>1</sup> C. J. Lewins,<sup>1</sup> P. R. Edwards,<sup>2</sup> R. W. Martin,<sup>2</sup> A. Šatka,<sup>3</sup>  
 D. W. E. Allsopp,<sup>1</sup> and P. A. Shields<sup>1,a)</sup>

<sup>1</sup>*Department of Electronic and Electrical Engineering, University of Bath, Bath BA2 7AY, United Kingdom*

<sup>2</sup>*Department of Physics, SUPA, University of Strathclyde, Glasgow G4 0NG, United Kingdom*

<sup>3</sup>*International Laser Centre, Ilkovicova 3, 84104 Bratislava, Slovak Republic*

(Received 19 April 2013; accepted 13 August 2013; published online 3 September 2013)

The use of etched nanorods from a planar template as a growth scaffold for a highly regular GaN/InGaN/GaN core-shell structure is demonstrated. The recovery of m-plane non-polar facets from etched high-aspect-ratio GaN nanorods is studied with and without the introduction of a hydrogen silsesquioxane passivation layer at the bottom of the etched nanorod arrays. This layer successfully prevented c-plane growth between the nanorods, resulting in vertical nanorod sidewalls ( $\sim 89.8^\circ$ ) and a more regular height distribution than re-growth on unpassivated nanorods. The height variation on passivated nanorods is solely determined by the uniformity of nanorod diameter, which degrades with increased growth duration. Facet-dependent indium incorporation of GaN/InGaN/GaN core-shell layers regrown onto the etched nanorods is observed by high-resolution cathodoluminescence imaging. Sharp features corresponding to diffracted wave-guide modes in angle-resolved photoluminescence measurements are evidence of the uniformity of the full core-shell structure grown on ordered etched nanorods. © 2013 AIP Publishing LLC.

[<http://dx.doi.org/10.1063/1.4819440>]

## I. INTRODUCTION

Obtaining a high density of high-aspect-ratio GaN nanorods is an essential first step in the growth and fabrication of a broad range of devices such as GaN/InGaN core-shell light-emitting diodes,<sup>1–6</sup> solar-cells,<sup>7</sup> and photodetectors.<sup>8</sup> Nanorod arrays aligned parallel to the c-axis support large-area active layers on the non-polar sidewalls. Quantum wells on these facets are free from the Quantum Confined Stark Effect<sup>9</sup> and potentially have reduced numbers of stacking faults compared with planar non-polar heteroepitaxial films.<sup>10</sup> This may lead to increased radiative recombination, the opportunity for thick quantum wells and reduced droop.<sup>11</sup> In addition, strain can be more easily relaxed through the high surface-to-volume ratio without the generation of crystal defects. Such GaN nanorod arrays can be created by bottom-up growth either through a self-organised or selective area growth process.<sup>12,13</sup> Alternatively, a top-down anisotropic etch process can create nanorods from a planar template.<sup>14,15</sup> This has the benefit of delivering greater uniformity at the expense of (1) possibly introducing etch-related roughness and damage, and (2) being limited by the quality of the original planar template. For the latter, it is not clear that pre-existing threading dislocations will influence the internal quantum efficiency of active layers grown on the non-polar sidewalls due to their predominant alignment along the polar c-axis.<sup>16</sup> Furthermore, we have previously demonstrated that the radiative efficiency in GaN nanorods up to 5  $\mu\text{m}$  in length formed by top-down processing is not necessarily degraded by etching.<sup>14</sup> The remaining issue of

surface roughness can be resolved by combining the top-down etch process with subsequent re-growth.<sup>5,17</sup> A schematic overview of the bottom-up and the combined approach as used in this paper is shown in Figure 1.

It remains a challenge to fabricate electrically driven nanorod arrays into devices that take advantage of all their opportunities. Ideally, device fabrication of nanorod-based devices should exploit existing and established processing techniques by converting from the three-dimensional to a planar geometry. Two methods for achieving this have typically been used to create devices based on an axial current flow. In the first, nanorods etched from a conventional planar light emitting diode (LED) have been fabricated into electroluminescent devices by planarizing with a filling material, exposing the nanorod tips and depositing a transparent conductor.<sup>19,20</sup> In the second method, semiconductor growth has been used to coalesce neighbouring nanorod tips into a planar layer for contacting.<sup>21,22</sup> For core-shell arrays, the current path in the active region is in the radial direction and parallel to the axis within the core and outer shell. Similar fabrication approaches as for axial current devices can be used provided that special attention is paid to the core and outer shell conductivity. Kölper *et al.*<sup>23</sup> describe a thin-film fabrication process for a core-shell nanorod LED in which the inter-rod space is filled with dielectric and a planar metal layer over the top of the rods provides contact to the p-type shell material and reflects light back down the nanorods to extract light through the n-type GaN buffer layer. For such structures, the growth of the active shell material will introduce variations in the size of the nanorods, making the planarization step and thus fabrication of devices more difficult. Ideally, a regular arrangement of vertically aligned GaN nanorods, with a well-defined homogeneity of height and

<sup>a)</sup>Author to whom correspondence should be addressed. Electronic mail: p.shields@bath.ac.uk.

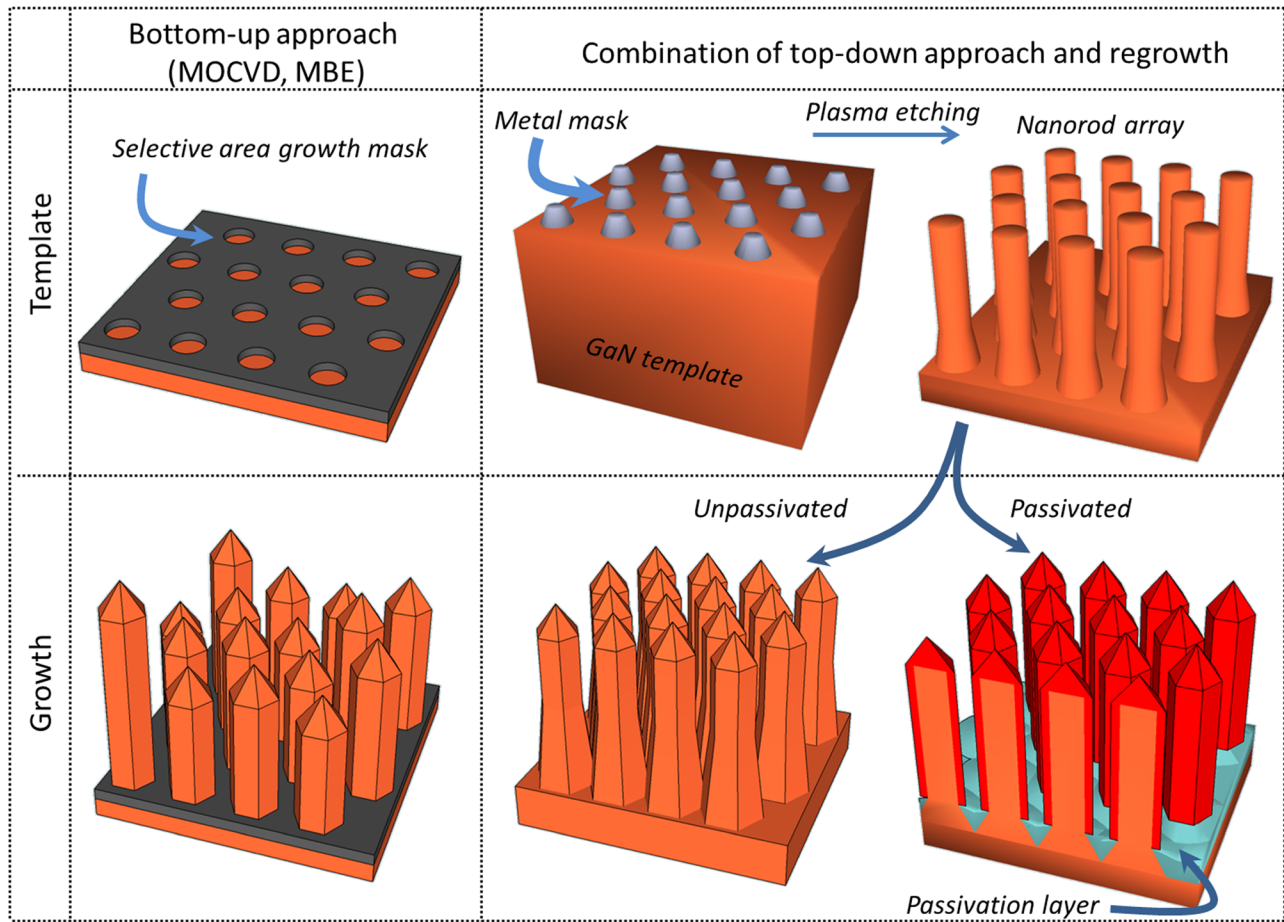


FIG. 1. Comparison of bottom-up and top-down core-shell fabrication processes. The bottom-up approach results in high-quality nanorods but with inhomogeneous height variation.<sup>18</sup>

width is required prior to the active layer growth. Achieving this with a bottom-up approach alone is challenging and as a result to date there are few reports of electrically driven arrays of core-shell devices and demonstrations of electrically connected core-shell structures are limited to single devices.<sup>4</sup> Hence, there has been recent interest in combining top-down etching and re-growth.<sup>5,17</sup>

Previously, we have demonstrated the etching of arrays of GaN nanorods from a planar GaN/sapphire template with an aspect ratio greater than 20 and, critically, negligible reduction in radiative efficiency.<sup>14</sup> The nanorods had an almost vertical sidewall and have been created across a 4 in. wafer using a metal dot array created by nanoimprint lithography and lift-off.<sup>24</sup> The height regularity of the nanorods is only limited by the roughness and long-range flatness of the original planar template. Therefore, the nanorods could act as a scaffold for the subsequent re-growth of shell layers via Metal Organic Vapour Phase Epitaxy (MOVPE) but this is not a well-established process.<sup>5,25</sup> A particular issue is the surface roughness of the nanorod sidewalls introduced by the dry-etch process. Thus, a preliminary growth step is required to recover the shape and facet structure of the nanorods prior to the growth of any active layer (Figure 1).

For application as a growth scaffold, such nanorods should be etched only part way into the GaN template in order to retain a conducting n-GaN layer so that the nanorods

can be electrically contacted in parallel. This leaves a number of competing surfaces, convex and concave, for the subsequent re-growth<sup>24</sup> in contrast with a bottom-up approach in which the growth mask prevents c-plane growth from the regions around the base of the nanorods. The blocking of this growth mode forces growth on the non-polar nanorod sidewalls and at the nanorod tip. A dielectric selective growth mask has a further benefit for device fabrication as it prevents current flow short-circuiting the core material.

Creating a similar growth mask for etched nanorods is a challenge since it must be added after the etching step. Conventional techniques such as evaporation, sputtering, and chemical vapour deposition preferentially deposit material near the tops of the nanorods. Whilst atomic layer deposition is a conformal process even for high-aspect-ratio structures,<sup>27</sup> none of these techniques allow preferential deposition at the nanorod bases to enable a reliable growth-blocking layer to be created. In this paper, we describe a procedure for creating a thin continuous passivation layer around the base of the nanorods using spin-on-glass and demonstrate its effect on the re-growth of GaN facets by MOVPE on high-aspect-ratio etched GaN nanorods. Recovery of the nanorod morphology is obtained. Statistical information on widths and heights show that the homogeneity of the starting etched nanorod scaffold is largely retained and it is shown that the approach results in the formation of highly ordered arrays of InGaN/GaN core-shell

nanorods, which display photonic crystal structure effects in their light emission.

## II. EXPERIMENTAL PROCEDURE

### A. Nanorod etching

GaN nanorod arrays have been created by a top-down approach from  $\sim 6\ \mu\text{m}$ -thick MOVPE-grown c-plane GaN on sapphire templates. A nickel-based metal mask was created using a nanoimprint lithography lift-off technique.<sup>24</sup> This resulted in a hexagonal array of metal nano-dots of 280 nm diameter and 600 nm pitch. The nanorod array was etched in an inductively coupled plasma (ICP) dry etch system (Oxford Instruments System 100) using parameters previously reported.<sup>14</sup> Figure 2 shows cross-section and plan views of an etched GaN nanorod array, which has a height of  $\sim 4\ \mu\text{m}$  and a density of  $\sim 3 \times 10^8\ \text{cm}^{-2}$ . The upper 80%–90% of the nanorods is vertical, whilst the lower 10%–20% displays a widening towards their base. Approximately  $2\ \mu\text{m}$  planar GaN remained below the nanorods. The cross-sectional image clearly shows the surface roughness that this work addresses.

### B. Nanorod passivation

*FOX*<sup>®</sup> Flowable Oxide (Dow Corning) is a liquid solution of hydrogen silsesquioxane (HSQ) in a carrier solvent that, after curing at high temperature, forms a robust, amorphous,  $\text{SiO}_2$ -like inorganic film, which can act as a selective growth mask in GaN epitaxy, similar to the  $\text{SiN}_x$  and  $\text{SiO}_2$  layers used in conventional epitaxial lateral overgrowth.<sup>28</sup> The effect of spin-coating on to an etched nanorod array depends on the solution viscosity. High viscosity layers can be used for infilling the spaces between nanorods to create nanorod LEDs using the planarizing properties of HSQ,<sup>19</sup> whereas solutions of low viscosity result in layers in which their morphology is dominated by surface tension. In the case of high-aspect-ratio nanorods, this leads to a thicker layer of material at the nanorod bases than on the top or sidewalls, as shown in Figure 3. This unique ability to coat preferentially the nanorod bases can be exploited in combination with a controlled buffered oxide wet-etch to create a passivation layer. This approach has also been used to prevent re-growth between nanorods during nanopendecol coalescence.<sup>29</sup>

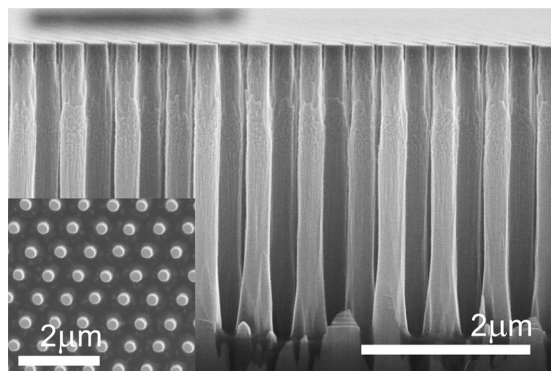


FIG. 2. Representative cross-sectional SEM image of the etched GaN nanorod array used throughout this paper. (Inset) Plan view SEM image of the nanorod array.

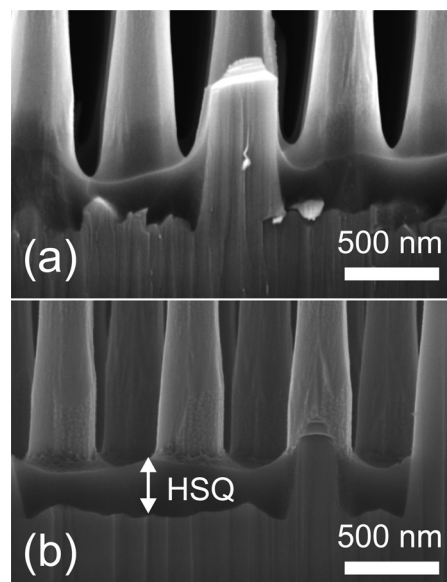


FIG. 3. Cross-sectional SEM images (at 5 kV) of the region near the nanorod bases for nanorods that have been coated with HSQ and subsequently cured at  $550\ ^\circ\text{C}$  for 2 h (a) without and (b) with subsequent wet-etching using 100:1 buffered oxide etch for 20 s.

The controlled etching of sub-100 nm layers of HSQ has been reported by Tiron *et al.*<sup>30</sup> By using a long ( $>120$  min) cure at  $550\ ^\circ\text{C}$ , the etch rate in dilute HF solution was reduced by an order of magnitude to  $\sim 10$  nm/min. This low etch rate allows the precise removal of cured HSQ from the nanorod sidewalls and tops whilst retaining a sufficient layer at the nanorod bases to act as a selective growth mask. Dilute HF does not etch GaN due to its high chemical stability.<sup>31</sup> Figure 3(a) shows an SEM image of the nanorods in Figure 2 after coating with HSQ (XR-1541e-beam resist (6%) from Dow Corning). It was spin-coated onto the bare rods at 3000 rpm. A subsequent  $200\ ^\circ\text{C}$  hotplate bake for 3 min removed the solvent and a further  $550\ ^\circ\text{C}$  bake in  $\text{N}_2$  atmosphere in a quartz tube furnace for  $\sim 2$  h cured the HSQ to reduce the etch rate. The thickness of the cured HSQ layer near the nanorod bases was  $\sim 2$ – $3$  greater than the thickness that would have been deposited on a planar sample. The coating tapered off up the sides of the nanorods as shown by the change in contrast in Figure 3(a).

After an etch in 100:1 buffered oxide etch solution, the passivation on the sides of the nanorods is removed leaving a layer intact at the base. The SEM image in Figure 3(b) shows a sharp transition between the HSQ and the nanorod, which is indicative of complete removal of the passivation from the sides of the nanorods. As will be seen, subsequent selective epitaxial growth on the nanorod sidewalls confirmed this interpretation of Figure 3(b).

## III. RESULTS AND DISCUSSION

### A. Semiconductor re-growth

To investigate the effect of the passivation on GaN re-growth, nanorods passivated with HSQ were wet etched with a 100:1 Buffer Oxide Etch (BOE) solution for different durations: 0, 20, 60, and 300 sec. MOVPE growth of GaN

was carried out simultaneously on all samples (growth temperature of 860 °C, growth pressure of 100 mbar, TMGa flow of 9 sccm, and NH<sub>3</sub> flow of 2800 sccm). Figure 4 shows SEM cross-sectional images after 30 min re-growth for the different etch durations. No growth occurs on the sample where the HSQ has not been wet-etched, indicating that the nanorod sidewalls and tops were fully covered with a thin HSQ layer. For the 20, 60, and 300 s duration etches, re-growth occurred along the full length of the nanorods to reveal {1–100} m-plane facets on the sidewalls and {10–11} facets on the nanorod tops to form nanopyramids.<sup>32</sup>

The passivation has a striking impact on the geometry of the re-grown GaN. At the bottom of the nanorods of the 60-s- and 300-s-etched samples, the verticality inherent to m-plane growth is lost. Other facets have formed or stepped growth has occurred to result in a departure from verticality. This enlargement at the bottom is ascribed to a complete removal of the HSQ layer during the wet-etch. In contrast, straight hexagonal-shaped nanorods were regrown on the 20-s-etched sample. M-plane facets are formed all along the nanorod, which is a potential asset for non-polar, core-shell devices. Therefore, the passivation layer inhibits formation of non-m-plane facets at the base of the nanorods during the re-growth and thus reduces irregularity in their final shape.

In Secs. III B–III D, the effect of the passivation layer on the distribution of nanorod diameters, verticality and heights after GaN re-growth onto high-aspect-ratio nanorods is described before progressing to the optical properties of InGaN shell growth onto such structures in Secs. III F and III G.

## B. Nanorod diameter and shape homogeneity

Any variation in diameter between nanorods could impact the emission behaviour in any core-shell structure since it could affect the homogeneity of the active layers. Any variation in height will increase the difficulty of subsequent device processing. Both could prevent their application in devices that exploit photonic crystal effects.

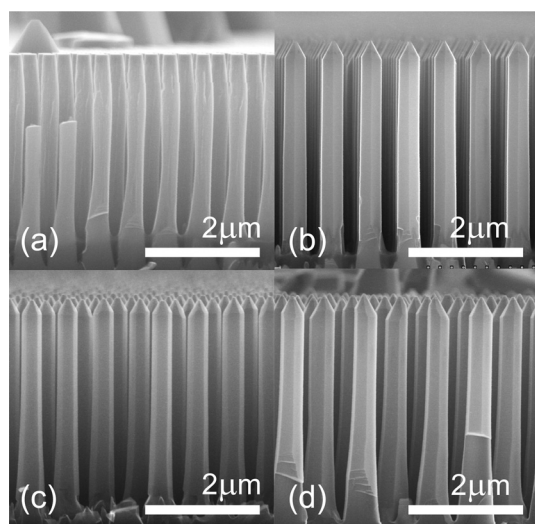


FIG. 4. Cross-sectional SEM images of 30 min GaN re-growth on HSQ-coated and cured GaN nanorod array exposed to BOE 100:1 solution for (a) 0 s, (b) 20 s, (c) 60 s, and (d) 300 s.

Passivated and unpassivated samples taken from the same etched nanorod wafer were simultaneously regrown for either 30 or 60 min, giving an increase in diameter of approximately 20% and 30%, respectively. The measured diameters were extracted from high-resolution SEM images. The high contrast in these images between the inclined nanopyramid facets and the nanorod sidewalls leads to an accurate size measurement of the nanorod top. Each 5000 $\times$ -magnification image contained around 1000 nanorods so that meaningful statistical distributions could be obtained. Similar SEM images of higher magnification are shown in Figures 5(a) and 5(b) for the 60 min growth. Figure 6 shows histograms of the measured diameters of both the passivated and unpassivated samples, whilst Figure 7 shows similar graphs for the elongation factor.<sup>33</sup> The distribution of these parameters is a measure of the uniformity of the nanorods and can be represented in a single value by the interdecile range (IDR); the separation of the 10% and 90% quantiles. This does not assume a particular probability density function.

GaN re-growth for 30 min led to an average increase of 61 nm in diameter for the passivated nanorods, whilst 60 min resulted in an increase of 106 nm. These values are consistent, to within 10%, with a constant rate of increase in added volume of material on the nanorod sidewalls. For the same growth time, the increase in diameter of the tops of the nanorods for the unpassivated samples was lower due to a greater deposition of material around the lower regions of the nanorods as seen from Figure 5(d).

It is expected that any irregularity in the nanorods formed during the etch process will be accentuated during the re-growth leading to inhomogeneity in the height, width, and shape due to the random growth nucleation or as a result of the growth dynamics. Nevertheless, direct re-growth on etched nanorods is still likely to provide better homogeneity than with a bottom-up approach alone. The dispersion in diameter (interdecile range) for the etched nanorods was found

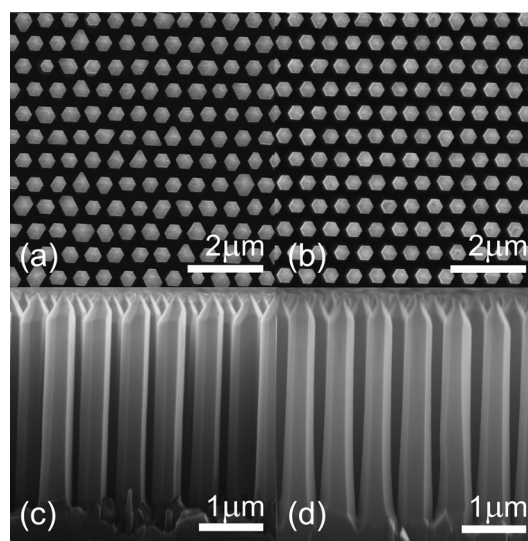


FIG. 5. Plan view and cross-sectional SEM images of 60 min GaN re-growth on passivated ((a) and (c)) and unpassivated ((b) and (d)) GaN etched nanorod array.

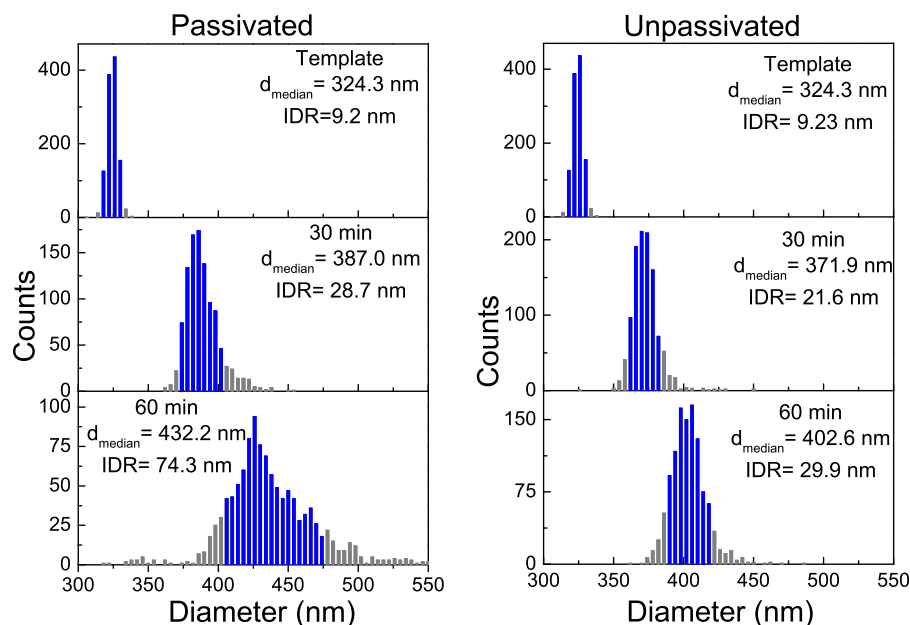


FIG. 6. Distribution of nanorod tip equivalent diameters as determined from 5000 $\times$ -magnification plan-view SEM images. The interdecile range is indicated in blue.

to be 9.2 nm, a variation of approximately 3% on the mean diameter. This reflects the precise size control that can be achieved with nanoimprint lithography and ICP etching. As expected, the dispersion was found to increase with subsequent growth. At first sight, it might seem that the passivation has increased the non-uniformity of the nanorods. However, a plot of the distribution width versus diameter (Figure 8(a)) reveals that there is monotonic increase in distribution width regardless of whether there is passivation or not. Indeed, the data suggest a linear dependence on diameter over the range of 325–400 nm. The datum outside this range, corresponding to the nanorods in Figures 5(a) and 5(c), possibly suggests that as the nanorods become wider the remaining space between them becomes a critical factor influencing the capture of material out of the gas phase in the growth reactor. The variation in the distribution of the elongation factors follows a similar trend, though the data indicate that the passivation has degraded the uniformity. A larger elongation

factor arises when the nanorods deviate from being hexagonal by the uneven growth rate of the six *m*-plane facets. The authors believe that there is a greater influence of the lower widened regions of the nanorods for the passivated samples leading to a greater range of elongation factors than for the unpassivated samples. Figure 2 shows that these widened regions are less uniform than the more vertical upper regions that were measured from the plan-view SEM images. Section III C, covering the nanorod verticality, will discuss this issue further.

### C. Nanorod verticality

The verticality of the nanorod sidewalls can be seen more clearly from the data summarized in Figure 9. This shows the average sidewall profile measured from the cross-sectional SEM images superimposed onto the average nanorod diameter as found from the diameter distributions in

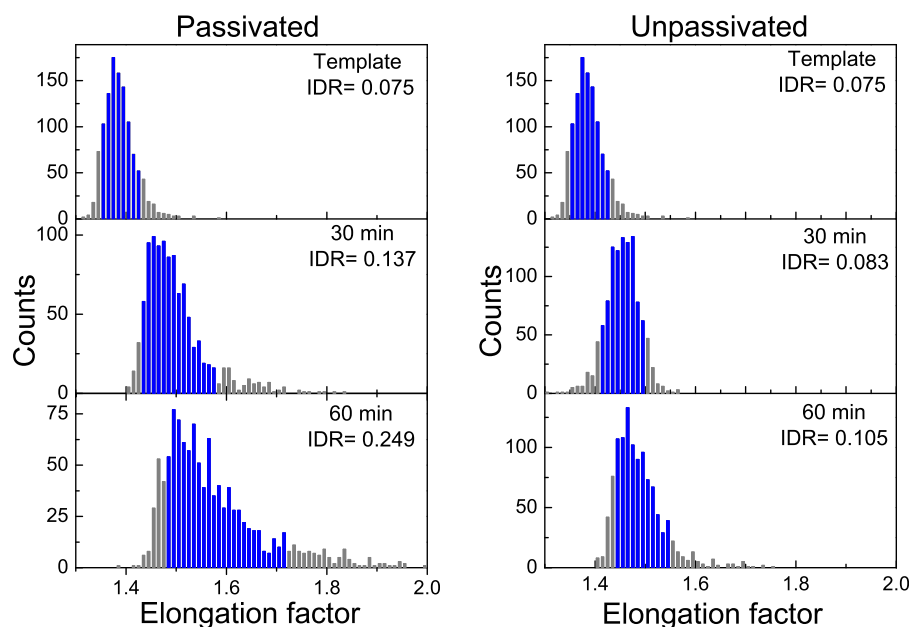


FIG. 7. Distribution of nanorod tip elongation factors as determined by image analysis of 5000 $\times$ -magnification plan-view SEM images. The elongation is a measure of the deviation in equivalent circularity corresponding to deviation from the hexagonal symmetry, where a perfect circle corresponds to a value of 1.27. The interdecile range is indicated in blue.

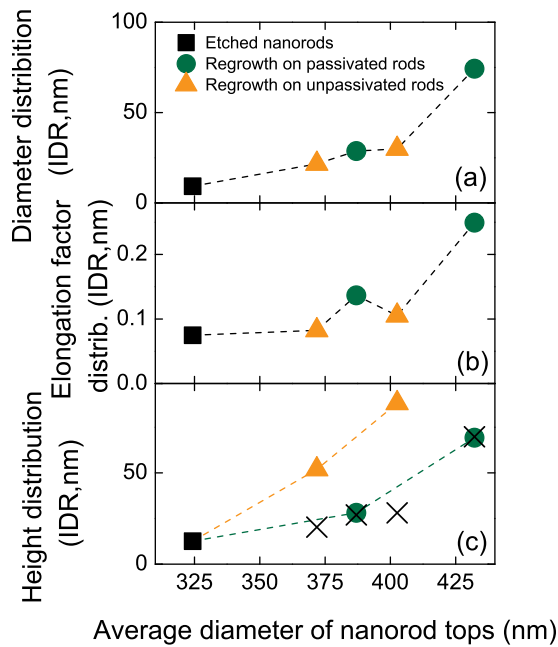


FIG. 8. The interdecile range of the nanorod diameter, elongation factor, and height versus average nanorod tip diameter showing that the passivation has no influence on the diameter distribution but has a significant influence on the height distribution. The crosses in (c) indicate the expected height variation as determined by the diameter variation assuming the nanorods are topped by a {10-11}-faceted nanopyramid (see Sec. III D for details).

Figure 6. This highlights the superior verticality of the sidewalls of the passivated samples compared with the unpassivated ones, which are substantially broadened over a region around their bases. The profile of the bare rods highlights the wine-glass shape that can just be discerned in Figure 2. The

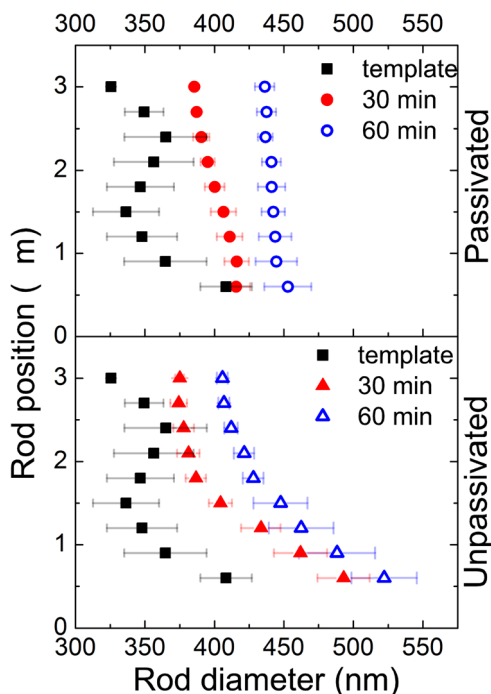


FIG. 9. Plot of the average rod diameter at different heights measured from the rod base for passivated and unpassivated nanorods for 0 min, 30 min, and 60 min GaN growth as determined from analysis of cross-sectional SEM images.

sidewall tapers outwards near the top of the rods before reducing to a waist region 1–2  $\mu\text{m}$  below the nanorod top. Near the base of the nanorods, there is a pronounced increase in the diameter. For the passivated samples, re-growth removes the wine-glass shape and gradually increases the verticality with 60 min ( $\sim 89.9^\circ$ ) being more vertical than 30 min ( $\sim 89.7^\circ$ ). In contrast, for the unpassivated samples, more growth *reduces* the verticality. The transition between vertical and truncated regions on the sidewalls of the unpassivated nanorods moves upwards with further growth, from approximately half way up for the 30 min sample to within 500 nm of the top for the 60 min sample. Blocking the growth at the bottom with a passivation layer causes the morphology to be determined by the slow-growing m-plane facets. Without a passivation layer, faster-growing high-index planes propagate up from the nanorod bases, overgrowing the m-planes. However, the drawback of the passivation is the increased influence of the less-uniform widened nanorod bases on the elongation factor as discussed in Sec. III B.

#### D. Nanorod height homogeneity

In order to assess the height distribution of the nanorods, AFM measurements have been carried out on all samples using a standard AFM tip (Veeco SCM-PIC) in contact mode. Due to the sharp nanopyramid on the top of the regrown samples, the features observed are a convolution of the nanopyramid and AFM tip shapes. Therefore, the maximum height measured for each nanorod has been extracted from the AFM data in order to exclude the influence of the AFM tip. Surface maps for each sample and histograms of the height data are shown in Figure 10. As expected, the as-etched nanorods show a tight distribution with very little random fluctuation in height reflecting the low roughness and flatness of the starting template. With re-growth, any inhomogeneity in the as-etched nanorod diameter or in the formation of the m-plane sidewalls gives rise to a fluctuation in the size of the basal plane of the {10-11}-faceted nanopyramids simultaneously developing on the nanorod top surface. This in turn leads to a height variation,  $\Delta h$ , which can be estimated from the diameter variation,  $\Delta d$ , using  $\Delta h \sim \Delta d / 2 \tan \theta$ , where  $\theta$  is the angle of the {10-11} facet with the c-plane ( $\sim 62^\circ$ ). The crosses in Figure 8(c) indicate the expected height variation corresponding to the diameter variation from Figure 8(a) using this model. This can be contrasted with the height variation as measured from the histograms in Figure 10 and also shown in Figure 8(c). All parameter variations are given for the interdecile range.

There is a striking similarity between the expected and measured data for the passivated samples thus confirming the origin of the variation for these cases. More noticeable, however, is the difference for the unpassivated samples. Such an increase in height variation does not correlate with either the diameter or elongation, both of which would influence the nanopyramid height as described above. The cause of the variation must arise from variability in the growth rate of the facets on top of the nanorod. Since the c-plane growth is usually much faster than the {10-11} growth, one can assume that the nanopyramid forms in the very early stages

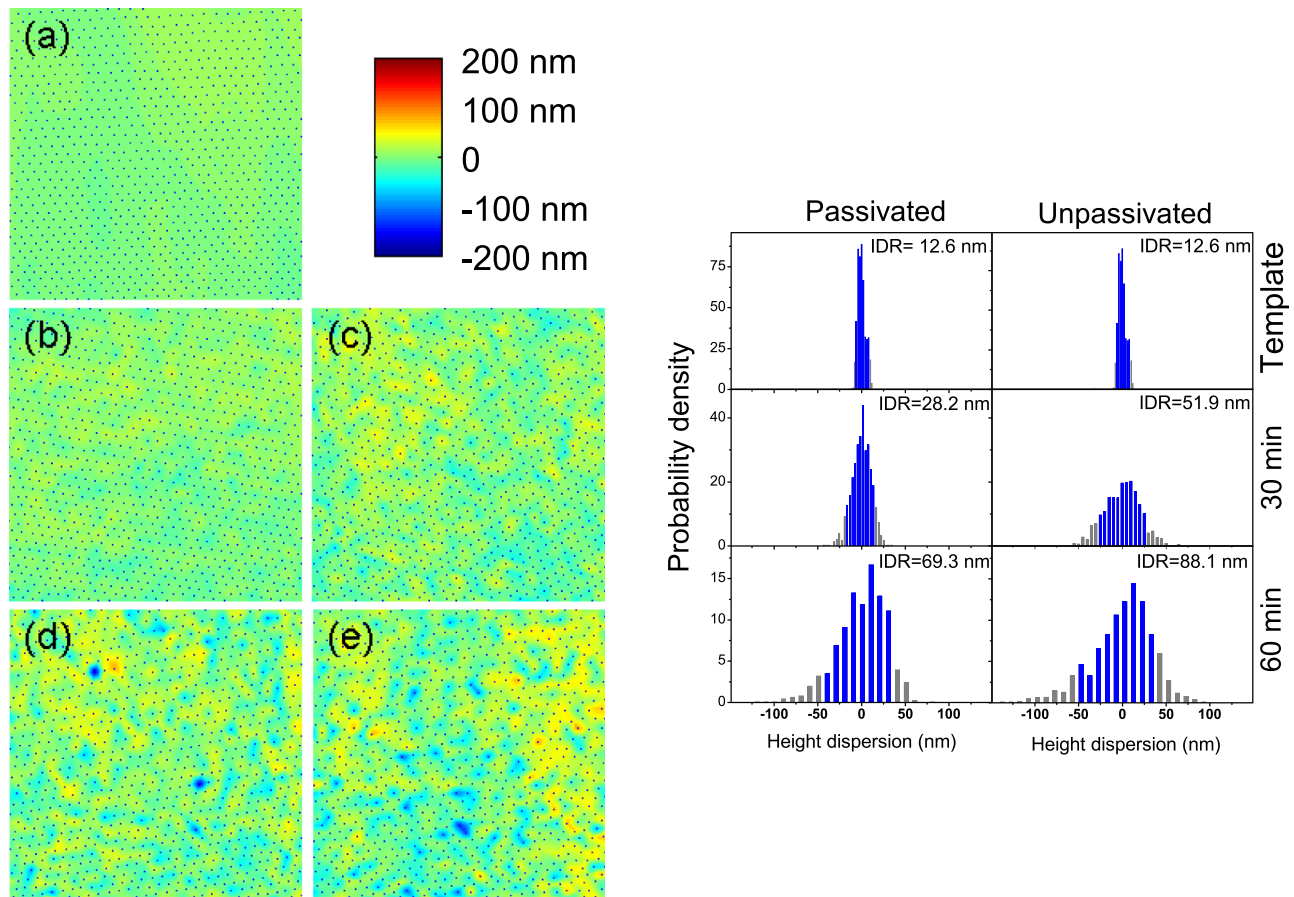


FIG. 10. (Left) Surface maps ( $19 \times 19 \mu\text{m}$ ) showing the nanorod heights for (a) bare nanorods, (b) passivated 30 min re-growth, (c) unpassivated 30 min re-growth, (d) passivated 60 min re-growth, (e) unpassivated 60 min re-growth as determined by AFM after a second-order polynomial background removal. The colour scale is the same for all images and the dots mark the x-y positions of the individual nanorod height maxima used to create the surface map. (Right) Histogram showing distribution of nanorod heights for each sample. The interdecile range is indicated in blue.

of growth,<sup>26</sup> thus leaving the  $\{10\text{--}11\}$  facets as the only ones remaining with a vertical growth rate component. So the question arises as to why the unpassivated nanorods give rise to a variable growth rate on these facets from one nanorod to another, whilst the passivated nanorods give rise to a constant growth rate. The most likely explanation is that the inhomogeneity present in the lower regions of the nanorods is affecting the surface diffusion of gallium from the sidewalls to the nanopyramid facets, and thus their growth rate. This is because the high-index facets or multiple step edges give rise to a dissimilar sidewall sticking coefficient from nanorod to nanorod. In contrast, the sidewalls of all passivated nanorods quickly develop into uniform m-plane facets. Thus, the transport of gallium from the slow-growing m-plane to the  $\{10\text{--}11\}$  facets is uniform between nanorods and, in turn, the variability in the height of the nanopyramid only reflects the uneven nanorod diameter.

These results demonstrate the advantage of using a passivation layer to improve the height uniformity of nanorods for subsequent processing into three-dimensional devices. In this case, the variability in height is solely attributed to the variation in the size of the nanopyramid basal plane, which degrades non-linearly with growth time. An interdecile range less than 30 nm for the height variation can be achieved if the increase in diameter is limited to 60 nm. More experiments are required to determine how much further the

diameter can increase before the height variation diverges catastrophically. Further improvement in height variation could be achieved by blocking the formation of the nanopyramid on the nanorod tip.

### E. Nanorod strain relaxation

To determine the strain status of the templates, the Raman spectra of the planar template, etched nanorods, and the nanorods after the GaN re-growth were compared (Figure 11). An accurate measurement of the position of the  $E_{2h}$  peak can reveal the modification of strain occurring in a GaN sample. Using a 532 nm laser, a shift of  $-1.9 \text{ cm}^{-1}$ , from  $569.2 \text{ cm}^{-1}$  to  $567.1 \text{ cm}^{-1}$ , was measured when the planar GaN template was etched. Such a shift can be ascribed to the relaxation of the compressive strain that exists in GaN/sapphire due to their lattice mismatch and different thermal expansion coefficients.<sup>34</sup> During cool down from the growth temperature, sapphire contracts faster than GaN leading to a build-up of compressive stress in the epilayer. The measured  $E_{2h}$  value of  $567.1 \text{ cm}^{-1}$  is close to that in strain-free GaN<sup>35</sup> indicating that the nanorods are fully relaxed prior to re-growth, in agreement with earlier findings.<sup>36</sup> Re-growth of GaN onto the etched nanorods does not re-introduce strain, as the  $E_{2h}$  peak remains in the same position at  $567.1 \text{ cm}^{-1}$ .

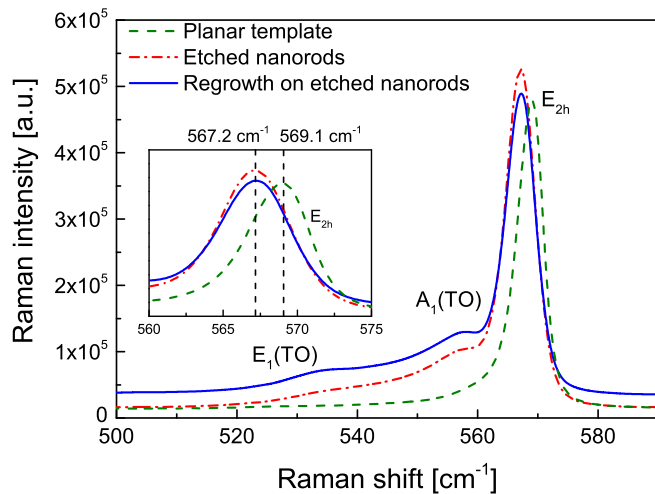


FIG. 11. Raman spectra of planar, etched, and 20-s-regrown samples recorded with a 532 nm laser. The inset shows a magnified view of the  $E_{2h}$  peak.

### F. GaN/InGaN/GaN core-shell optical properties

In order to further examine the quality of the nanorod templates and their suitability for device structure growth, a GaN/InGaN/GaN core-shell active layer was prepared on the nanorod templates by MOVPE. Shorter etched nanorods with regrown facets were over-grown with InGaN (growth temperature 750 °C, growth pressure of 300 mbar, TMGa flow rate of 9 sccm, TMIIn flow rate of 360 sccm, and  $\text{NH}_3$  flow rate of 5 slm) followed by a GaN capping layer at the same temperature. The smaller aspect ratio leads to a greater increase in the diameter for the same growth time. Figure 12 shows the regrowth of GaN/InGaN/GaN on nanorods with an approximate height of (a) 700 nm, and (b) 400 nm. The SEM images clearly show a sharp boundary separating the passivation layer and the bottom part of the re-grown structure.

High-resolution cathodoluminescence (CL) hyperspectral imaging at 5 keV accelerating voltage has been used to

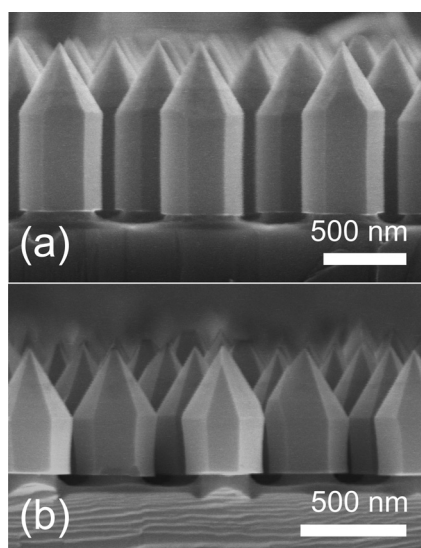


FIG. 12. (a) and (b) SEM images showing examples of active GaN/InGaN/GaN layers regrown on shorter etched nanorods clearly highlighting the effect of the passivation layer.

characterise the optical properties of the GaN/InGaN/GaN core-shell structures, shown in Figure 12(b). This technique measures the full emission spectrum from successive localised regions determined by the probing volume of the electron beam in order to build up a multi-dimensional dataset containing spatial and spectroscopic information of the sample.<sup>37</sup> The geometry is such that the sample is at 45° to the electron beam and 45° to the optical detection axis. All spectra have been obtained at room temperature. The secondary electron and corresponding CL images and spectra are shown in Figure 13. The dotted lines trace the outline of the nanostructure and are useful to highlight that the brightest luminescence originates from the region where the vertical facets intersect with the {10–11} facets of the nanopyramid. Figure 13(b) shows the real colour of the overall emission as determined from the chromaticity coordinates for each spectrum, whilst Figure 13(d) shows normalised individual spectra originating from different regions of the nanostructure.

An analysis of all such spectra leads to the identification of three separate emission bands centred at around 2.5, 3.2, and 3.4 eV. The false colour map in Figure 13(c) reveals that the three bands in different colours, highlighted in Figure 13(d), clearly originate from separate regions of the nanostructure: strong GaN near band-edge light is emitted from the centre of the nanopyramid facets; the 3.2 eV peak originates from the vertical m-plane facets, and the broad band around 2.5 eV is emitted from the intersection between these facets. The latter two peaks are attributed to emission from  $\text{In}_x\text{Ga}_{1-x}\text{N}$  with different alloy composition,  $x$ . The emission peak energy can then be used to estimate the alloy

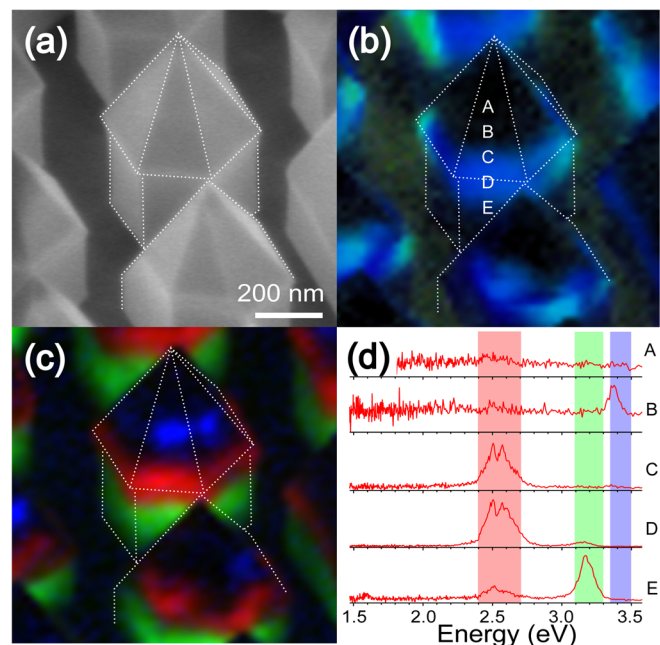


FIG. 13. (a) SEM secondary electron image of the GaN/InGaN/GaN layers regrown on shorter etched nanorods and (b) corresponding CL map of the optical emission from the active layers. The colour in (b) represents the real emission colour as determined from the chromaticity coordinates calculated for each spectrum. A selection of normalised individual spectra corresponding to positions A-E is shown in (d). The false colour CL map in (c) highlights the spatial origin of the optical emission corresponding to the three identified bands (red, green, and blue) as shown in (d).

composition in the separate regions by referring to published values from InGaN films, neglecting any quantum confinement or electric field effects.<sup>38</sup> This gives values of  $x \sim 5\%$  for the vertical m-plane emission and  $x \sim 20\%$  for the region intersecting the m-plane and  $\{10\text{--}11\}$  facets. The spectra in Figure 13(d) also show that the broad 2.5 eV emission band consists of more than one peak. Whilst the same emission band is observed in other neighbouring nanorods, the relative strength of the individual constituent peaks varies, which is likely a geometric effect.

The  $\sim 5\%$  indium incorporation on the m-plane is consistent with previous work that found a low incorporation rate on this facet in comparison with other semi-polar facets.<sup>39</sup> It is more surprising that no InGaN emission is observed from the  $\{10\text{--}11\}$  facets. Only GaN near-band edge light is emitted in a central band around the middle of the nanopyramid semi-polar facet, with no emission observed nearer the nanopyramid tip. CL is not a confocal spectroscopy technique so the spatial diffusion of carriers to regions of lower band-gap cannot explain the lack of emission. Instead, the dark tip results from competing non-radiative recombination routes via defects at the nanopyramid tip introduced during their growth.<sup>40</sup>

Another important feature of the spectra in Figure 13(d) is the lack of luminescence at 2.2 eV, attributed to the defects in GaN structures. The negligible luminescence in this band clearly proves a high quality core-shell structure, confirming also the high quality of the nanorod template.

### G. Angular dependence of emission

Angle-resolved photoluminescence (PL) experiments were performed in order to study the impact of the high degree of ordering and shape regularity of the core-shell nanorods. The PL was excited by a 405 nm diode laser that

was focussed to a spot size  $<1$  mm so that only the broad InGaN band at  $\sim 2.5$  eV is excited. The emission was detected using a fibre goniometer connected to a spectrograph and CCD detector. The fibre bundle, positioned at a distance of 300 mm away from the sample, was moved in  $0.1^\circ$  steps away from the surface normal and in the azimuthal directions in order to build up a complete solid angle of measurements over, in principle, a full hemisphere. One “slice” from the multi-dimensional dataset corresponding to a single azimuth is shown in Figure 14(a). In order to highlight the diffraction features, the PL data have been normalised to the emission band along the y-axis, and to the integrated intensity along the x-axis. The emission band at normal incidence is shown in Figure 14(b), and the angular emission at a single wavelength of 510 nm (pre-normalisation), corresponding to the emission band peak is shown in Figure 14(c).

Figure 14(a) is characterised by an array of features corresponding to diffraction from the nanorod array combined with lines delineating regions of higher and lower intensities that define triangular-like sectors. Light that is emitted into the laterally guided modes of the whole GaN layer (nanorods plus residual GaN template) is diffracted into the extraction cone. This appears as a set of sharp lines in the angular emission spectrum where each line corresponds to diffraction from an allowed mode. A further wave-guiding effect occurs with light that is primarily trapped in the sapphire substrate. Due to the large substrate thickness, the spacing of these diffraction lines is too small to resolve. Instead, they appear as an increase in the background intensity of the extracted light in the triangular sectors, for example, below  $45^\circ$  at  $\sim 500$  nm. For further details of photonic crystal extraction, see, for example, Refs. 41 and 42.

Both diffraction pathways and corresponding light extraction derive from the high degree of long-range order

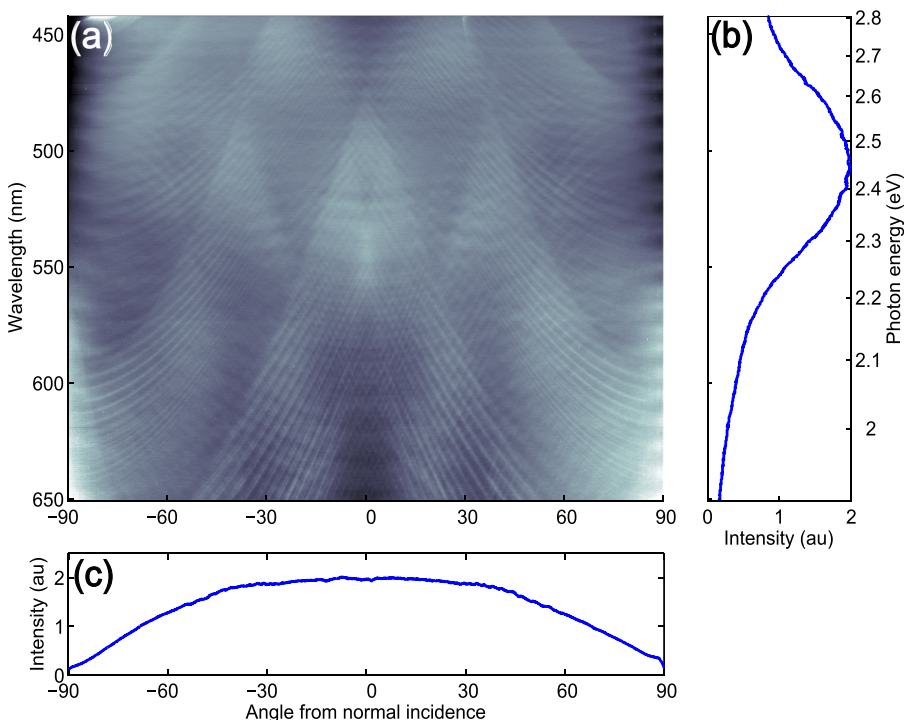


FIG. 14. (a) Horizon-to-horizon angle-resolved PL emission from the GaN/InGaN/GaN core-shell structure shown in Figure 12(b). The data have been normalised along the vertical axis to the PL emission band and along the horizontal axis to the average intensity at that elevation in order to highlight the diffractive features. (b) Normal incidence PL spectrum and (c) angular emission at 510 nm.

that is present within this core-shell nanorod array. This in turn results from the top-down approach used to create the initial GaN nanorod scaffold before the facet recovery step and the re-growth of the active layers.

#### IV. CONCLUSION

In conclusion, we have demonstrated a two-step process that leads to the availability of a high-aspect-ratio nanorod array with very high uniformity that could be used as a growth scaffold for core-shell light-emitting devices. The rough morphology introduced in the first etch step is repaired during a subsequent re-growth step in which the m-plane crystal facets are recovered.

The controlled deposition and etching of a layer of HSQ onto the nanorods prior to the re-growth step is described. This passivation layer has a number of benefits: (1) it reduces the variation of nanorod heights by a factor of two, thus making nanorod and prospective core-shell devices easier to realise, (2) it increases the verticality of the nanorods, ensuring fully non-polar side walls, (3) it prevents parasitic c-plane growth between the nanorods, and (4) it acts to block parasitic current paths that bypass the nanorod core.

The characterisation of emission from an active InGaN layer grown on top of the nanorods shows (1) strong localisation of the emission as a result of differing alloy compositions in different regions and (2) sufficient long-range order to observe increased light extraction through the diffraction of trapped modes within the high-refractive index GaN or sapphire layers.

#### ACKNOWLEDGMENTS

The authors would like to thank OSRAM Opto Semiconductors GmbH for the provision of the GaN/sapphire templates and acknowledge financial support from the European Union (FP7 Contract No.: 228999, “SMASH”) and the EPSRC, UK via Grant No. EP/I012591/1 “Lighting the Future.”

- <sup>1</sup>C.-H. Liao, W.-M. Chang, Y.-F. Yao, H.-T. Chen, C.-Y. Su, C.-Y. Chen, C. Hsieh, H.-S. Chen, C.-G. Tu, Y.-W. Kiang, C. C. Yang, and T.-C. Hsu, *J. Appl. Phys.* **113**, 054315 (2013).
- <sup>2</sup>S. Li, X. Wang, S. Fundling, M. Erenburg, J. Ledig, J. Wei, H. H. Wehmann, A. Waag, W. Bergbauer, M. Mandl, M. Strassburg, A. Trampert, U. Jahn, H. Riechert, H. Jonen, and A. Hangleiter, *Appl. Phys. Lett.* **101**, 032103 (2012).
- <sup>3</sup>T.-W. Yeh, Y.-T. Lin, L. S. Stewart, P. D. Dapkus, R. Sarkissian, J. D. O'Brien, B. Ahn, and S. R. Nutt, *Nano Lett.* **12**, 3257 (2012).
- <sup>4</sup>A. Waag, X. Wang, S. Fundling, J. Ledig, M. Erenburg, R. Neumann, M. Al Suleiman, S. Merzsch, J. Wei, S. Li, H. H. Wehmann, W. Bergbauer, M. Straßburg, A. Trampert, U. Jahn, and H. Riechert, *Phys. Status Solidi C* **8**, 2296 (2011).
- <sup>5</sup>J.-R. Chang, S.-P. Chang, Y.-J. Li, Y.-J. Cheng, K.-P. Sou, J.-K. Huang, H.-C. Kuo, and C.-Y. Chang, *Appl. Phys. Lett.* **100**, 261103 (2012).
- <sup>6</sup>H. Sekiguchi, K. Kishino, and A. Kikuchi, *Appl. Phys. Express* **1**, 124002 (2008).
- <sup>7</sup>J. J. Wierer, Q. Li, D. D. Koleske, S. R. Lee, and G. T. Wang, *Nanotechnology* **23**, 194007 (2012).
- <sup>8</sup>A. D. L. Bugallo, L. Rigutti, G. Jacopin, F. H. Julien, C. Durand, X. J. Chen, D. Salomon, J. Eymery, and M. Tchernycheva, *Appl. Phys. Lett.* **98**, 233107 (2011).
- <sup>9</sup>P. Waltereit, O. Brandt, A. Trampert, H. Grahn, J. Menniger, M. Ramsteiner, M. Reiche, and K. Ploog, *Nature* **406**, 865 (2000).

- <sup>10</sup>Q. Sun and J. Han, *GaN and ZnO-Based Materials and Devices*, edited by S. Pearton, Springer Series in Materials Science (Springer, 2012), Vol. 156, pp. 1–27.
- <sup>11</sup>S.-C. Ling, T.-C. Lu, S.-P. Chang, J.-R. Chen, H.-C. Kuo, and S.-C. Wang, *Appl. Phys. Lett.* **96**, 231101 (2010).
- <sup>12</sup>S. Li and A. Waag, *J. Appl. Phys.* **111**, 071101 (2012).
- <sup>13</sup>K. Kishino, H. Sekiguchi, and A. Kikuchi, *J. Cryst. Growth* **311**, 2063 (2009).
- <sup>14</sup>P. Shields, M. Hugues, J. Zúñiga-Pérez, M. Cooke, M. Dineen, W. Wang, F. Causa, and D. Allsopp, *Phys. Status Solidi C* **9**, 631 (2012).
- <sup>15</sup>D. Paramanik, A. Motayed, G. S. Aluri, J.-Y. Ha, S. Krylyuk, A. V. Davydov, M. King, S. McLaughlin, S. Gupta, and H. Cramer, *J. Vac. Sci. Technol. B* **30**, 052202 (2012).
- <sup>16</sup>B. Heying, X. H. Wu, S. Keller, Y. Li, D. Kapolnek, B. P. Keller, S. P. Den Baars, and J. S. Speck, *Appl. Phys. Lett.* **68**, 643 (1996).
- <sup>17</sup>S. Krylyuk, D. Paramanik, M. King, A. Motayed, J.-Y. Ha, J. E. Bonevich, A. Talin, and A. V. Davydov, *Appl. Phys. Lett.* **101**, 241119 (2012).
- <sup>18</sup>B. Mattias Borg, J. Johansson, K. Storm, and K. Deppert, *J. Cryst. Growth* **366**, 15 (2013).
- <sup>19</sup>Y. D. Zhuang, C. J. Lewins, S. Lis, P. A. Shields, and D. W. E. Allsopp, *IEEE Photon. Technol. Lett.* **25**, 1047 (2013).
- <sup>20</sup>Y.-H. Ra, R. Navamathavan, J.-H. Park, and C.-R. Lee, *ACS App. Mater. Interfaces* **5**, 2111–2117 (2013).
- <sup>21</sup>K. Kishino, J. Kamimura, and K. Kamiyama, *Appl. Phys. Express* **5**, 031001 (2012).
- <sup>22</sup>A.-L. Bavecove, G. Tourbot, E. Pugeoise, J. Garcia, P. Gilet, F. Levy, B. André, G. Feuillet, B. Gayral, B. Daudin, and L. S. Dang, *Phys. Status Solidi A* **207**, 1425 (2010).
- <sup>23</sup>C. Kölper, M. Sabathil, F. Römer, M. Mandl, M. Strassburg, and B. Witzigmann, *Phys. Status Solidi A* **209**, 2304 (2012).
- <sup>24</sup>P. A. Shields and D. W. E. Allsopp, *Microelectron. Eng.* **88**, 3011 (2011).
- <sup>25</sup>N. A. Fichtenbaum, C. J. Neufeld, C. Schaake, Y. Wu, M. H. Wong, M. Grundmann, S. Keller, S. P. DenBaars, J. S. Speck, and U. K. Mishra, *Jpn. J. Appl. Phys., Part 2* **46**, L230 (2007).
- <sup>26</sup>D. Du, D. Srolovitz, M. Coltrin, and C. Mitchell, *Phys. Rev. Lett.* **95**, 155503 (2005).
- <sup>27</sup>J. W. Elam, D. Routkevitch, P. P. Mardilovich, and S. M. George, *Chem. Mater.* **15**, 3507 (2003).
- <sup>28</sup>P. Gibart, *Rep. Prog. Phys.* **67**, 667 (2004).
- <sup>29</sup>P. A. Shields, C. Liu, A. Šatka, A. Trampert, J. Zúñiga-Pérez, B. Alloing, D. Haško, F. Uherek, W. Wang, F. Causa, and D. Allsopp, *Phys. Status Solidi C* **8**, 2334 (2011).
- <sup>30</sup>R. Tiron, L. Mollard, O. Louveau, and E. Lajoinie, *J. Vac. Sci. Technol. B* **25**, 1147 (2007).
- <sup>31</sup>D. Zhuang and J. H. Edgar, *Mater. Sci. Eng. R.* **48**, 1 (2005).
- <sup>32</sup>C. Liu, P. A. Shields, Q. Chen, D. W. E. Allsopp, W. N. Wang, C. R. Bowen, T.-L. Phan, and D. Cherns, *Phys. Status Solidi C* **7**, 32 (2010).
- <sup>33</sup>The elongation factor is defined as the ratio of the line segment, which connects the two furthest apart points and the shortest side of an equivalent area rectangle.
- <sup>34</sup>L. T. Tung, K. L. Lin, E. Y. Chang, W. C. Huang, Y. L. Hsiao, and C. H. Chiang, *J. Phys.: Conf. Ser.* **187**, 012021 (2009).
- <sup>35</sup>V. Laneuville, F. Demangeot, R. Péchou, P. Salles, A. Ponchet, G. Jacopin, L. Rigutti, A. De Luna Bugallo, M. Tchernycheva, F. Julien, K. March, L. Zagonel, and R. Songmuang, *Phys. Rev. B* **83**, 115417 (2011).
- <sup>36</sup>M. Hugues, P. A. Shields, F. Sacconi, M. Mexis, M. Auf der Maur, M. Cooke, M. Dineen, A. Di Carlo, D. W. E. Allsopp, and J. Zuniga-Perez, *J. Appl. Phys.* **114**, 084307 (2013).
- <sup>37</sup>P. R. Edwards and R. W. Martin, *Semicond. Sci. Technol.* **26**, 064005 (2011).
- <sup>38</sup>K. O'Donnell, R. Martin, C. Trager-Cowan, M. White, K. Esona, C. Deatcher, P. Middleton, K. Jacobs, W. Van der Stricht, C. Merlet, B. Gil, A. Vantomme, and J. F. Mosselmans, *Mater. Sci. Eng., B* **82**, 194 (2001).
- <sup>39</sup>Y. Zhao, Q. Yan, C.-Y. Huang, S.-C. Huang, P. Shan Hsu, S. Tanaka, C.-C. Pan, Y. Kawaguchi, K. Fujito, C. G. Van de Walle, J. S. Speck, S. P. DenBaars, S. Nakamura, and D. Feezell, *Appl. Phys. Lett.* **100**, 201108 (2012).
- <sup>40</sup>C. Liu, A. Šatka, L. K. Jagadamma, P. R. Edwards, D. Allsopp, R. W. Martin, P. Shields, J. Kovac, F. Uherek, and W. Wang, *Appl. Phys. Express* **2**, 121002 (2009).
- <sup>41</sup>A. David, H. Benisty, and C. Weisbuch, *Rep. Prog. Phys.* **75**, 126501 (2012).
- <sup>42</sup>C. J. Lewins, D. W. E. Allsopp, P. A. Shields, X. Gao, B. Humphreys, and W. N. Wang, *J. Disp. Technol.* **9**, 333 (2013).